

DNA Closed Nanostructures: A Structural and Monte Carlo Simulation Study

Francesca Baldelli Bombelli,[†] Filippo Gambinossi,[†] Marco Lagi,[†] Debora Berti,[†]
Gabriella Caminati,[†] Tom Brown,[‡] Francesco Sciortino,[§] Bengt Nordén,^{||} and Piero Baglioni^{*,†}

Department of Chemistry and CSGI, University of Florence, Via della Lastruccia 3 - Sesto Fiorentino, 50019 Florence, Italy, School of Chemistry, University of Southampton, Highfield, Southampton SO17 1BJ, United Kingdom, Dipartimento di Fisica and Istituto Nazionale di Fisica della Materia, Università di Roma "La Sapienza", Piazzale Aldo Moro 2, I-00185 Rome, Italy, and Department of Chemical and Biological Engineering/Physical Chemistry, Chalmers University of Technology, SE-41296 Gothenburg, Sweden

Received: May 22, 2008; Revised Manuscript Received: August 10, 2008

DNA nanoconstructs are obtained in solution by using six unique 42-mer DNA oligonucleotides, whose sequences have been designed to form a pseudohexagonal structure. The required flexibility is provided by the insertion of two non-base-paired thymines in the middle of each sequence that work as flexible hinges and constitute the corners of the nanostructure when formed. We show that hexagonally shaped nanostructures of about 7 nm diameter and their corresponding linear open constructs are formed by self-assembly of the specifically designed linear oligonucleotides. The structural and dynamical characterization of the nanostructure is obtained in situ for the first time by using dynamic light scattering (DLS), a noninvasive method that provides a fast dynamic and structural analysis and allows the characterization of the different synthetic DNA nanoconstructs in solution. A validation of the LS results is obtained through Monte Carlo (MC) simulations and atomic force microscopy (AFM). In particular, a mesoscale molecular model for DNA, developed by Knotts et al., is exploited to perform MC simulations and to obtain information about the conformations as well as the conformational flexibilities of these nanostructures, while AFM provides a very detailed particle analysis that yields an estimation of the particle size and size distribution. The structural features obtained by MC and AFM are in good agreement with DLS, showing that DLS is a fast and reliable tool for characterization of DNA nanostructures in solution.

Introduction

DNA is a powerful building block for the production of digitally addressable nanomaterials of desired geometry and size with the highest information density available in Nature. The characteristic size domain and the geometrical and molecular recognition properties make DNA an ideal candidate for the construction of novel nanomaterials. Recently, molecular recognition properties displayed by amphiphilic supramolecular assemblies, i.e., phospholiponucleosides^{1–6} and polyelectrolytes (DNA, RNA), have been exploited for the construction of novel complex nanostructures.⁷ DNA has been shown to be able to self-assemble in predefined 3D geometries^{8–11} and in ordered 2D nanoarrays,^{12–17} exploitable as scaffolding materials in nanotechnology. Large efforts in the synthetic bottom-up strategy based on DNA self-assembly are currently devoted to develop new nanosized motifs, namely, subunits, able to hierarchically organize in preprogrammed ordered arrays with high addressability.^{18–23} The structural properties of these subunits, such as shape, size, flexibility, and so forth, are of paramount importance and inherently determine the features of the nanodevice at the mesoscale. Despite the important steps done in the development of DNA-based complex nanostructures

and in their self-organization, not much is known about the physicochemical properties of these subunits. Gel electrophoresis and atomic force microscopy (AFM) are popular techniques to detect and show complex DNA nanostructures: Gel electrophoresis is the most used tool to verify the final products by comparison with the intermediate ones, while AFM is very useful in providing high spatial resolution images of DNA nanostructures and their periodic 2D arrays. However, neither of these approaches can give information about the structural and dynamical properties of the nanostructured units in their bulk medium, since once self-assembled, they have to be transferred into gels or deposited on a surface to be characterized. Moreover, AFM structural analysis requires a large number of measurements and the analysis of several images to be representative of the sample. The characterization of these nanostructures in solution, in terms of structure, flexibility, stability, and tendency to aggregate, is crucial in the perspective to bind them, through base-pairing, to soft and hard particles for the construction of ordered assembly patterns.^{24–28} Fluorescence resonance energy transfer (FRET) experiments²⁹ and cryo transmission electron microscopy¹⁰ (Cryo-TEM) have previously been used to get structural information on DNA-based nanostructures in the bulk, but also in these cases, either addition of fluorescence probes or vitrification process is needed, respectively.

Dynamic light scattering (DLS) represents a noninvasive technique that allows a fast dynamic and structural analysis of nanosized particles in situ. An ensemble-averaged representative distribution of the particles as a function of their center-of-mass diffusion (or of their hydrodynamic radii) is obtained in a single

* Mailing address: Prof. Piero Baglioni, Department of Chemistry & CSGI, University of Florence, Via della Lastruccia 3, 50019, Sesto Fiorentino, Florence, Italy. Telephone: +39-055-4573033. Fax: +39-055-4573032. E-mail: baglioni@csgi.unifi.it.

[†] University of Florence.

[‡] University of Southampton.

[§] Università di Roma "La Sapienza".

^{||} Chalmers University of Technology.

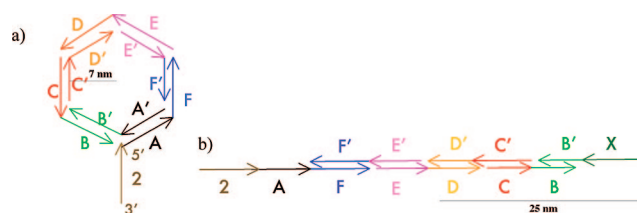


Figure 1. Schematic drawing of the DNA nanostructures obtained by mixing the strands reported in Table 1 in TRIS buffer solution. (a) Closed DNA nanostructure (by mixing 1–6A strands). (b) Linear open DNA nanostructure (by mixing 1–6B strands without 6A). The dimensions are estimated through simple geometrical calculations.

experiment. From these data, one can retrieve information about the particles' structural parameters and detect polymerization or aggregation products, even if present in low percentages in solution. However, the complete analysis of dynamic light scattering data requires the knowledge of the shape of the particles in solution, especially in the presence of more than one particle population. Hence, it is important to have an interpretative tool to evaluate the structure of complex DNA-based nanostructures with different geometries. A computer modeling approach able to predict the shape of complex DNA self-assemblies represents a relatively inexpensive and fast way to optimize new fundamental motifs in the perspective to build more complex and versatile nanoarrays. A computational shape-based approach has been developed for proteins, where the desired shape drives the choices of the building-blocks.³⁰ This was very recently applied to RNA to design all possible structures of RNA nanoparticles capable of siRNA delivery, showing the high potentialities of such a method in the field of bionanotechnology.³¹

In this contribution, we report a dynamic light scattering investigation of closed DNA nanostructures and of their open linear analogues in solution. These structures were obtained by using six unique, 42-mer DNA oligonucleotides, whose sequences are designed to form a pseudohexagonal structure, with rigid sides composed of 20-mer double strands and edges formed by a nonpairing TT sequence. The same approach has been exploited previously in order to obtain a predesigned construct composed of six different DNA double helices.²⁹ These DNA architectures (see Figure 1) are decorated by a DNA sticky-end (single strand labeled 2 in Figure 1) intended as an anchoring site for programmable surface immobilization or tethering to soft supports.²⁴ In this perspective, a clear in situ distinction between the closed nanoconstructs from possible byproduct (such as the open linear analogue or possible polymerization products) becomes mandatory. We provide a dynamic and structural characterization of these nano-objects, giving the size distribution of the different structures in solution and highlighting the presence of possible aggregation or polymerization products. The experimental findings have been compared to the structural parameters predicted with Monte Carlo simulations, performed using a mesoscale molecular model for DNA, developed by Knotts et al.,³² to reproduce the conformations and the conformational flexibilities of our nanostructures. UV-melting behavior of these nanostructures in solution has also been studied. Finally, we have also performed an AFM study of the same samples analyzed with DLS, to characterize the nanostructures in the direct space. A detailed particle analysis of the AFM images has provided an estimation of the particle size distribution on the surface, and possible structural modifications, due to the deposition on the surface, have also been detected by comparison with the DLS size distribution.

TABLE 1: DNA Strands

list	name	sequence
1	FA-2	5'-ACGAGCCTTTGACGCTTGGA-TT-TAGTGCCTAACATAGGCTAC-TT-CTGAAATTATGATAAAGA-3'
2	F' E'	5'-ATTTACCTGGAAGCAGCCAC-TT-TCCAAGCGTCAAAGGCTCGT-3'
3	DE	5'-GTGGCTGCTTCCAGGTAAA-TT-CACTATGTAACCTGGTCTCTTA-3'
4	D'C'	5'-TAGAGACCAGTTACATAGTG-TT-TGACCTCAGTCGCAAGGCTG-3'
5	BC	5'-CAGCCTTGCGACTGAGGTCA-TT-TCGGGTCAACGAATGGCTGC-3'
6A	B'A'	5'-GCAGCCATTCGTTGACCCGA-TT-GTAGCCTATGTTACGCACTA-3'
6B	B'X	5'-GCAGCCATTCGTTGACCCGA-TT-CCCCCCCCCTTTTTTTTTT-3'

Materials and Methods

1. Sequence Design. The linear DNA oligonucleotide (ODN) building blocks 1–6A, reported in Table 1, have been designed to form hexagonally shaped DNA self-assemblies in aqueous solution with 7 nm rigid sides connected by flexible joints (Figure 1a). The required flexibility is provided by the insertion of two non-base-paired thymines in the middle of each sequence that work as flexible hinges and constitute the corners of the nano-object when it is formed. The corresponding open nanostructure (Figure 1b) was obtained by substituting strand 6A with 6B, thus removing the possibility for the structure to close up.

2. Synthesis and Purification of DNA. Standard deoxyribonucleoside phosphoramidite monomers, solid supports, and additional reagents for oligonucleotide synthesis were purchased from Link Technologies and Applied Biosystems. All oligonucleotides were synthesized on an Applied Biosystems 394 automated DNA/RNA synthesizer using a standard 0.2 μ mol phosphoramidite cycle of acid-catalyzed detritylation, coupling, capping, and iodine oxidation. Stepwise coupling efficiencies and overall yields were determined by the automated trityl cation conductivity monitoring facility and in all cases were >98.0%. Cleavage of oligonucleotides from the solid support and deprotection were achieved by exposure to concentrated aqueous ammonia solution for 60 min at room temperature followed by heating in a sealed tube for 5 h at 55 °C.

The oligonucleotides purified on a Gilson HPLC system using a Brownlee Aquapore RP-HPLC column (8 mm \times 25 cm, Perkin-Elmer). The HPLC system was controlled by Gilson 7.12 software, and the following protocol was used: run time = 24 min; integration time = 21 min; flow rate = 4 mL per min; binary gradient of buffers A and B: Time in min (% buffer B), 0 (0), 3 (0), 4 (10), 17 (40), 19 (100), 20 (100), 21 (0), 24 (0). Elution buffers: A = 0.1 M aqueous NH_4OAc pH 7, B = 0.1 M aqueous NH_4OAc with 50% acetonitrile pH 7. Elution of oligonucleotides was monitored by ultraviolet absorption at 297 nm.

3. Sample Preparation. The concentration of each ODN was set using near neighboring approximation (NNA) values for the extinction coefficients and their absorbance at 260 nm. The nanostructures have been formed in 50 mM TRIS buffer (pH = 7.5) with 100 mM NaCl by mixing equimolar amounts of the DNA sequences for a 3 μ M final concentration of each strand in solution, which means a 3 μ M concentration of the nanoconstructs. The samples used for all the experiments have been annealed by heating to 90 °C and then cooled to 5 °C with a constant temperature gradient over 6 h.

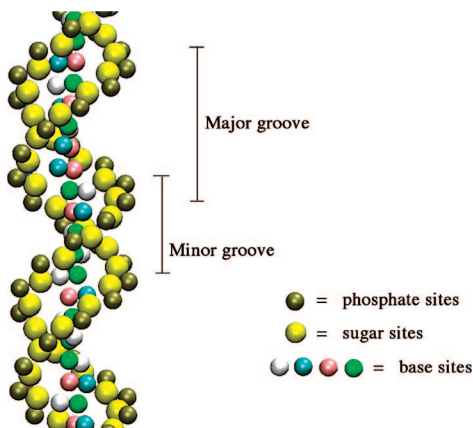


Figure 2. Representation of the DNA mesoscopic model.

4. Monte Carlo Simulations (MC). Only a few mesoscopic models are able to describe DNA melting and/or hybridization^{33,34} containing Coulomb interactions at the same time. Since both these features should be considered to properly compare simulations and experiments on DNA, we select the recently proposed off-lattice model.³² This model reasonably reproduces the melting/hybridization temperature (within ± 10 K) of ds-DNA polynucleotides including the screening effect of salts and the major/minor grooving of DNA. Here, we provide only a brief description of the model: additional information can be found in the original article.

Each nucleotide is coarse-grained as a three-site group: one site for phosphate (placed at its center of mass), one for the sugar (placed at its center of mass), and one for the base (placed at N1 or N3 position, for purines and pyrimidines, respectively). A graphic representation of the model is reported in Figure 2. The potential energy of the system V_{total} is composed of seven terms:

$$V_{\text{tot}} = V_{\text{bond}} + V_{\text{angle}} + V_{\text{dihedral}} + V_{\text{stack}} + V_{\text{bp}} + V_{\text{ex}} + V_{\text{qq}} \quad (1)$$

The first three terms are the contributions for intramolecular degrees of freedom as bonds, angles, and dihedrals, and these parameters are chosen according to the crystallographic structure of double-stranded B-DNA.³⁵ The other four terms represent nonbonded interactions: V_{stack} is an intrastrand potential accounting for the base stacking and the backbone stiffness and is built according to the Go-type native contact scheme.³⁶ V_{bp} describes the hydrogen-bonded base pairing both intra- and interstrand. V_{ex} models the excluded volume interactions and V_{qq} the Coulombic ones, within the Debye–Huckel approximation. While the phosphate sites only contribute to the electrostatic term (or if they are located on two adjacent bases consecutive they are included in V_{angle}), the other three nonbonded potentials have a more complex structure since they are mutually exclusive; one couple of sites contributes to only one of these three terms and a *hierarchical approach* is adopted, checking first if a couple contributes to V_{stack} , then to V_{bp} , and the remaining couples are assigned to V_{ex} .

The Monte Carlo simulations were performed in an *NVT* ensemble at different temperatures (ranging from 10 to 90 °C). An MC step was defined as an attempt to move all sites in the system. The amplitude of the random translation is 0.4 Å. Simulations last for about 1×10^8 MC steps. Two different systems were investigated, namely, the closed and the linear open nanoconstructs described above (Figure 1, 42-mer nucleotide strands, I = ionic strength = 150 mM).

These systems were found to have very slow equilibration kinetics, and it was not possible to reproduce with simple MC moves the full hybridization processes.

Although the model is in principle capable of describing melting and hybridization, the hybridization process must overcome large free energy barriers (since the Debye–Huckel repulsion is much more long-range than the hydrogen bonding attraction). Hence, the adopted coarse-graining of the present 126 bp double-stranded system is still not sufficient to address the hybridization processes with our computational capabilities. We performed simulations of both systems at 20 and 70 °C but were only able to obtain an evaluation of the equilibrium conformation of the constructs for the former temperature, since at this temperature, only the double-stranded state is sampled with a reasonable statistical weight. In the studied time window, at high temperature (70 °C) we observed an incomplete melting of starting double-stranded configuration, but we could not assess if the partially melted state is the equilibrium one. Moreover, the simulation of the two structures at 70 °C provided a representation of their thermal behavior and highlighted differences in their dissociation processes as explained later (see movie in the Supporting Information section). Monte Carlo simulations have also been performed on analogous smaller systems²⁹ (the total number of sites for the smaller systems - 22 DNA base - is 396, while for the 42 DNA bases it is 756), in order to validate our model in the case where it was possible to reproduce the complete melting process and compare it to the experimental melting data. In this case, the agreement between experimental melting temperatures and simulated ones is very good and within the expected uncertainty (see Supporting Information).

5. Dynamic Light Scattering (DLS). DLS experiments were performed on a Brookhaven Instrument apparatus, New York (BI9000AT correlator card and BI200SM goniometer). The signal was detected by an EMI 9863B/350 photomultiplier. The light source was the doubled frequency of a Coherent Innova diode pumped Nd:YAG laser, ($\lambda = 532$ nm, 20 mW). The laser long-term power stability was $\pm 0.5\%$. Self-beating detection was recorded using decahydronaphthalene (thermostatted by a water circulating system) as index matching liquid. A temperature probe was placed in the sample to monitor T while simultaneously recording autocorrelation functions. Measurements have been performed at 20 °C on 0.5 mL samples previously transferred into cylindrical Hellma cells and flushed with N_2 to avoid bubble formation. For each sample, at least two measurements were performed at seven different angles (i.e., 40°, 45°, 50°, 60°, 70°, 90°, and 120°, respectively) corresponding to seven different scattering vectors $q = 4\pi n/\lambda \sin(\theta/2)$; n is the refractive index of the medium equal to 1.33 and θ is the scattering angle. The acquisition time was 1 h for each measurement. Experiments were repeated on different DNA batches.

In dynamic light scattering experiments, the normalized time autocorrelation function $g_2(q, t)$ of the scattered intensity is measured according to

$$g_2(q, t) = \frac{\langle I^*(q, 0)I(q, t) \rangle}{\langle I(q, 0)^2 \rangle} \quad (2)$$

For ergodic systems, this function can be expressed in terms of the field autocorrelation function $g_1(q, t)$ through the Siegert relation

$$g_2(q, t) = A[1 + \beta^2 g_1(q, t)^2] \quad (3)$$

where A is the baseline and β^2 is the coherence factor dependent on the scattering geometry and details of the detection system.

Data analysis has been performed with two different methods: in the first one, the autocorrelation functions have been reproduced through a double exponential decay, yielding two distinct decay rates, labeled “fast” and “slow” decay modes. The same experimental data have been analyzed through Laplace inversion, according to the CONTIN algorithm,³³ to infer a distribution of the decay rates corresponding to the two populations.

In the first case, the analytical expression used to fit the field autocorrelation functions was

$$g_1(q, t) = A(Pe^{-\Gamma_1 t} + (1 - P)e^{-\Gamma_2 t}) + B \quad (4)$$

where A is the total amplitude of the correlation function, P is the contribution of the first mode to the total amplitude, and B is the baseline. This analysis, although neglecting polydispersity of the two populations, is a good control on the Laplace inversion method (CONTIN) that can produce, mostly with noisy intensity autocorrelation functions with low amplitude to baseline ratio, not genuine results.

When the spectral profile of the scattered light can be described by a multi-Lorentzian curve, then $g_1(q, t)$ can be written as the Laplace transform of the spectrum of relaxation times

$$g_1(q, t) = \int_0^\infty w(\tau) \cdot e^{-\frac{t}{\tau}} d\tau \quad (5)$$

τ is the relaxation time characteristic of the system and $w(\tau)$ is the intensity-weighted relaxation time distribution. In order to obtain a distribution $w(\tau)$ of decay rates, a constrained regularization method, CONTIN, was used to invert experimental data. A statistical parameter “probability to reject”, α , is calculated for each $w(\tau)$ generated by CONTIN. The preferred solution is usually the one characterized by the α value closest to 0.5.

6. Atomic Force Microscopy (AFM). Immobilization of DNA samples on a mica surface was achieved using divalent cations to bridge the phosphate groups of DNA to the negatively charged mica surface.^{37–39} Different immobilization protocols have been used in the past to produce AFM imaging of ds-DNA. Most of them are based on the pretreatment of the mica surface with cationic chemicals or silanes^{40,41} or on the physical adsorption from a DNA solution with both monovalent and divalent cations.^{37,39,42–44} Both procedures yield similar results and support the DNA binding to mica.^{38,45} However, it has been demonstrated that a development procedure consisting of rinsing with water⁴⁶ and the post ethanol treatment⁴⁷ increases the repulsion forces between DNA chains and enhances the stabilization of the double strands anchored on the mica surface. Stock solutions of 3 μ M DNA nanostructures were diluted to 1.7 μ M with 50 mM TRIS buffer (pH 7.5) and 1.0 mM Mg(OAc)₂ at a constant ionic strength $I = 0.15$ M. A 20 μ L aliquot was spotted onto a freshly cleaved mica surface (Agar Scientific) and left standing for about 10 min. The sample was then immersed in ultrapure water for 1 h, rinsed with anhydrous ethanol, and dried. Separate experiments with different starting concentrations indicated the optimal working concentration range for AFM imaging of the resulting structures to be 1–2 μ M.

AFM experiments were performed with a Park System XE-100 microscope (PSIA Inc., Korea) using new NCHR silicon cantilevers with 42 N/m spring constant and 320 KHz working frequency. The nominal curvature radius of the tip is 5 nm; special care was taken to use defect-free tips for each AFM run. A true noncontact AFM (NC-AFM) mode to preserve the

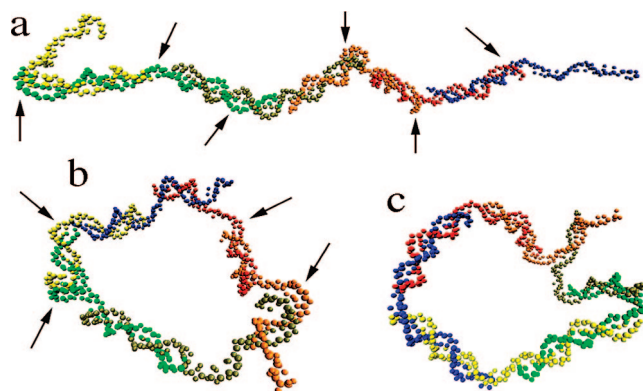


Figure 3. Equilibrium conformations of 42-mer ds-DNA nanostructures at 20 °C: (a) open construct (see Figure 1b) and (b) ring-like construct (see Figure 1a). Arrows point out the junctions, where the structures deviate from linearity due to flexibility imparted by the TT hinges. (c) Representation of a structural defect in the ring-like assembly.

TABLE 2: Average Structural Parameters Extracted from Monte Carlo Simulations

system	$\langle R_g \rangle$ (nm)	$\langle a \rangle$ (nm)	$\langle d_{cc} \rangle$ (nm)	$\langle \sigma_{ang} \rangle$ (°)	$\langle \sigma_{dih} \rangle$ (°)	D_t (cm ² s ⁻¹)
ring-like, 42-mer	7.3 ± 0.3	7.1 ± 0.1		22.5	40.5	2.80×10^{-7}
open, 42-mer	11.3 ± 0.3		44.3 ± 3.8			1.80×10^{-7}

integrity of the samples^{48,49} and avoid squeezing of the DNA assemblies has been used. All the images were recorded in air at room temperature and at a scan speed of 0.5–2 Hz. Phase and amplitude deflections as well as height and internal sensor images were collected simultaneously in both trace and retrace directions. Image processing and cross-sectional profiling were performed with WSxM software version 4.0 Develop 11.⁵⁰ Standard image processing consisted of plane subtraction and line-by-line flattening; a mathematical morphology method⁵¹ was used to remove the effect of tip broadening. Particle analysis was accomplished by using the public domain software *ImageJ*.⁵² Features due to the mica surface and single pixel noise were eliminated using the threshold function implemented in the software. The reported data are the average of multiple AFM experiments repeated for different DNA sample batches.

Surface density histograms were fitted to log-normal distribution functions:

$$\Gamma(R_m) = \Gamma_0 e^{\left\{ -\frac{\ln 2}{(\ln f)^2} \left[\ln \left(\frac{R_m - R_0}{w} \cdot \frac{f^2 - 1}{f} + 1 \right) \right]^2 \right\}}; \quad R_m > R_0 - \frac{wf}{f^2 - 1} \quad (6)$$

where $\Gamma(R_m)$ is the density of structures of a particular radius, Γ_0 is the maximum density of structures, R_0 is the mean radius, $w = R_r - R_l$ is the width at the half-maximum and $f = (R_r - R_0)/(R_0 - R_l)$ is a skewness estimate, related to the asymmetry of the log-normal distribution function. The parameters R_l and R_r are the radius at the half-maximum density on the left and right sides of the curve, respectively (see Supporting Information).

UV Melting. UV melting experiments were performed on a Cary 100 spectrophotometer (Varian) equipped with a temperature-controlled multicell block. The temperature gradient was 0.5 °C/min and the absorption was measured at $\lambda = 260$ nm. Samples were degassed under N₂ flow before measurement. The

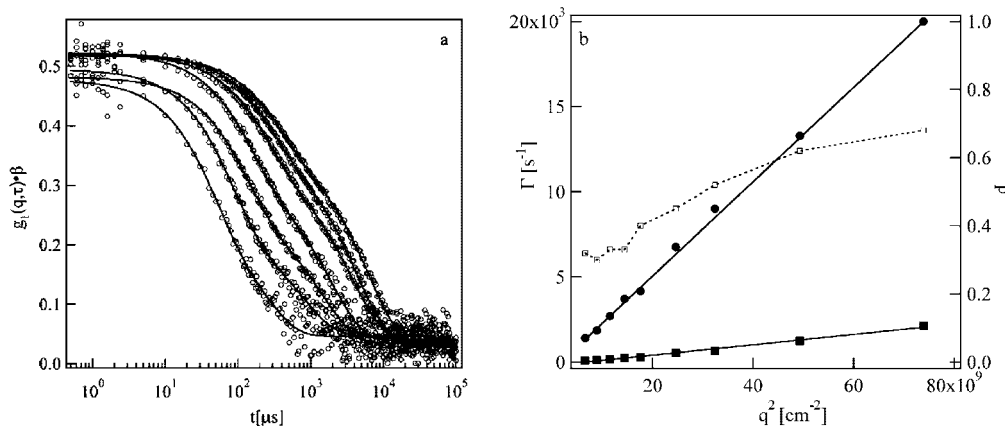


Figure 4. (a) DLS intensity autocorrelation functions of 3 μM DNA closed nanostructures at different scattering angles. The double exponential fitting (DEF) curves are reported as solid lines. (b) Behavior of the relaxation rates as a function of the square scattering vector. The decay rates are obtained through double exponential fitting according to eq 3. In the right y-axis, the intensity-weighted contributions, P , of the fast mode are reported. The solid lines are fitting to infer the translational diffusion coefficient $D_t = \Gamma/q^2$. (●) Γ_1 (fast mode), (■) Γ_2 (slow mode), (□) P .

first derivative of the curve was exploited to estimate the melting temperature T_m of the structures. Thermal heating/cooling cycles from 5 to 85 $^{\circ}\text{C}$ were repeated twice on the same sample to exclude hysteresis process.

Results

Monte Carlo Simulations. The equilibrium conformations at $T = 20$ $^{\circ}\text{C}$ of closed and linear nanostructures obtained by Monte Carlo simulations are reported in Figure 3. These images clearly show that the thymine hinges (indicated with black arrows) confer the desired high flexibility to these nano-objects affecting their overall structure. Table 2 reports the relevant average geometrical parameters, calculated from the simulated equilibrium structures. The radius of gyration, R_g , is evaluated for both systems, while the mean half-distance between opposite edges (thymine junctions), a , and the standard deviation from the mean value of the angle between three ($120^{\circ} \pm \sigma_{\text{ang}}$) and four ($0^{\circ} \pm \sigma_{\text{dih}}$, proper dihedral) consecutive thymine hinges are reported for the closed system. The end-to-end distance d_{ee} , defined as the distance between the first and the last base, is also shown for the linear open object.

The determined radius of gyration, R_g , of the simulated open structure is larger than that of the ring-like system. This is in agreement with the theoretical predictions for which the $\langle R_g \rangle$ of an ideal circular chain is smaller than that of a linear chain of the same contour length by a factor of $\sqrt{2}$.⁵³ The relation has been also extended for polymers with an excluded volume.⁵⁴ The mean end-to-end distance (Figure 3a) is shorter than the contour length of the corresponding rigid double strand (50 nm), indicating that the open construct is characterized by a relatively high flexibility, due to the TT junctions. For the same reasons, the closed structure cannot be considered a stiff planar hexagon in solution, as one can see from the relatively high standard deviations of corner angles and dihedral angles. Moreover, we frequently observe the formation of structural defects in the cyclic structure (Figure 3c), similar to what has previously been observed for different cyclic DNA systems.⁵⁵ These defects imply local dissociation of the DNA strands and a rearrangement of the involved chain in a nonplanar structure. The higher standard deviation for dihedral angles reflects the important role of the thymine junctions in the formation of these conformations.

Once these structural parameters are known, we can predict the dynamic behavior of these nanostructures in solution. In particular, modeling the ring-like object as a torus for which $R_g^2 = (a^2 + b^2)$,⁵⁶ where a and b are, respectively, the radius and the cross-sectional radius of the torus, we can calculate the translational diffusion coefficient, D_t , according to⁵⁷

$$D_t = \frac{k_B T}{8\pi^2 \eta_s a} \left(\log\left(\frac{8a}{b}\right) + \frac{1}{2} \right) \quad (7)$$

where η_s is the solvent viscosity, and k_B the Boltzmann constant. Substituting a and b with $\langle a \rangle$ and $(\langle R_g^2 \rangle - a^2)^{1/2}$ (Table 2), respectively, we obtain $D_t = 2.80 \times 10^{-7} \text{ cm}^2/\text{s}$.

For the open linear counterpart, the theory of dynamics of dilute polyelectrolyte solutions predicts, taking into account electrostatic, excluded volume and hydrodynamic interactions, a translational diffusion coefficient equal to⁵⁸

$$D_t = \frac{8\sqrt{2} k_B T}{3 \eta_s} \frac{1}{(12\pi^3 d^2 ee)^{1/2}} \quad (8)$$

where d_{ee} is the end-end distance of the polyelectrolyte chain. Substituting in eq 8 the $\langle d_{ee} \rangle$ inferred from the simulations, we obtain D_t equal to $1.80 \times 10^{-7} \text{ cm}^2/\text{s}$. These results indicate that these assemblies can be distinguished from the analysis of their diffusive behavior in solution.

Moreover, simulations of the response to a sudden T raise at 70 $^{\circ}\text{C}$ of both nanostructures equilibrated at 20 $^{\circ}\text{C}$ indicate that the opening of the ring and the initial melting of the linear structure always occur at the same 20-mer sequence, i.e., between the strands that are richer in A and T (DD' double strand for the 42-mer; see Table 1). This is expected and is due to the lower interaction energy for AT base pairs (2 H-bonds) with respect to GC base pairs (3 H-bonds). Other differences emerge from simulations that reproduce double-strand dissociation: chain melting starts at a lower temperature for the ring-like structure and induces a faster opening of the ring with respect to the breakup of the same duplex in the open nanostructure where this process occurs more slowly.

Dynamic Light Scattering. DLS experiments of 3 μM DNA closed objects in solution have been performed as a function of the scattering vector q in the range $(1.07\text{--}2.95) \times 10^5 \text{ cm}^{-1}$ at 20 $^{\circ}\text{C}$. The field autocorrelation functions reported in Figure 4a are bimodal; i.e., they are characterized by two sets of relaxation times. The decay rates obtained by fitting the

TABLE 3: Results from Double Exponential (DEF) and CONTIN Fittings of the Autocorrelation Functions at Different Scattering Angles for DNA Ring-Like and Open Nanostructures

	D_t^a [cm^2s^{-1}] double exponential fitting (DEF)	R_H^b [nm] DEF	$\langle D_t \rangle^c$ [cm^2s^{-1}] CONTIN	$\langle R_H \rangle^d$ [nm] CONTIN
ring-like fast	$2.93 \times 10^{-7} \pm 1.40 \times 10^{-8}$	7.5 ± 0.4	$2.76 \times 10^{-7} \pm 1.38 \times 10^{-8}$	7.8 ± 0.4
ring-like slow	$2.41 \times 10^{-8} \pm 3.50 \times 10^{-9}$	88.0 ± 13.0	$2.08 \times 10^{-8} \pm 3.20 \times 10^{-9}$	103.0 ± 15.8
open fast	$1.98 \times 10^{-7} \pm 1.21 \times 10^{-8}$	10.8 ± 1.0	$1.54 \times 10^{-7} \pm 1.18 \times 10^{-8}$	13.9 ± 1.3
open slow	$1.66 \times 10^{-8} \pm 3.03 \times 10^{-9}$	128.9 ± 23.5	$9.58 \times 10^{-9} \pm 1.24 \times 10^{-9}$	223.4 ± 28.9

^a D_t translational diffusion coefficient. ^b R_H hydrodynamic radius from eq 4. ^c $\langle D_t \rangle$ z -averaged collective diffusion coefficient. ^d $\langle R_H \rangle$ z -averaged hydrodynamic radius from eq 5.

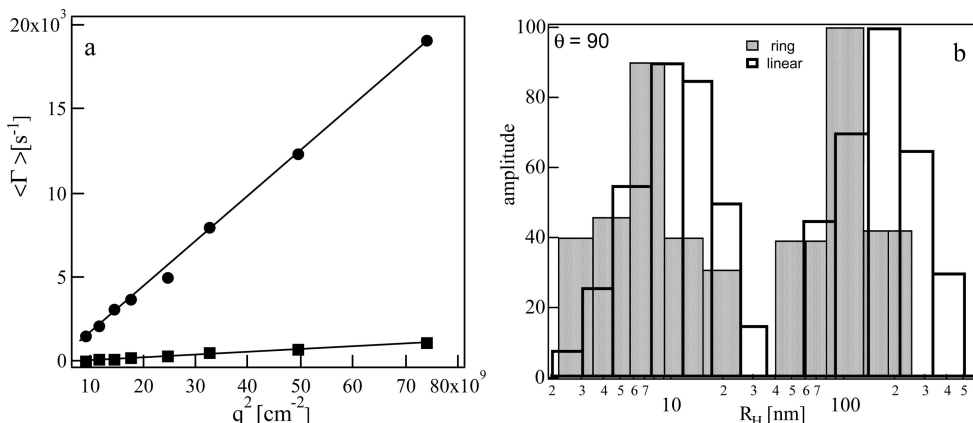


Figure 5. (a) Behavior of the average relaxation modes obtained by CONTIN as a function of the square scattering vector. The solid lines are the linear fittings to infer the average translation diffusion coefficient $\langle D_t \rangle = \langle \Gamma \rangle / q^2$. (●) Γ_1 (fast mode), (■) Γ_2 (slow mode). (b) Intensity-weighted distributions of the two relaxation mode populations obtained with the CONTIN procedure as a function of hydrodynamic radius for ring-like and open systems at $\theta = 90^\circ$.

autocorrelation functions with a double exponential function (DEF), reported in eq 4, are shown in Figure 4B. Both populations show a linear dependence of the decay rate vs the square scattering vector, q^2 , typical of a diffusive behavior.

The experimental fast diffusion coefficient shows a very good agreement with that predicted by the theory for ring-like nanostructures (Table 2), so the population contributing with fast relaxation times to concentration fluctuations can be unambiguously identified as closed DNA nanostructures.

The diffusion coefficients provide access to the hydrodynamic correlation lengths R_H for isotropic particles through the Stokes–Einstein relationship

$$D_t = \frac{k_B T}{6\pi\eta_s R_H} \quad (9)$$

where η_s is the solvent viscosity and k_B the Boltzmann constant. Both D_t and R_H are reported in Table 3. R_H of the fast population is of the same order of magnitude of the closed nanostructure size (Figure 1), while the size of the slow population is 1 order of magnitude larger.

The relative amplitude, P , of the fast mode is also reported in Figure 4B, as a function of the scattering vector. The contribution of this population is underestimated because the scattered intensity is proportional to the square of the mass of the particle.⁵⁹ Furthermore, the amplitude shows a clear dependence on the length scale investigated (q^{-1}); in particular, its value is maximum at a high q -value where the form factor contribution of the large particles vanishes.

The relaxation time distributions of the two populations can also be obtained by CONTIN inversion (see Materials and Methods section). The obtained z -averaged decay modes, $\langle \Gamma \rangle$, are reported as a function of the square scattering vector in Figure 5a. The average translational diffusion coefficients and the corresponding hydrodynamic lengths for the two populations

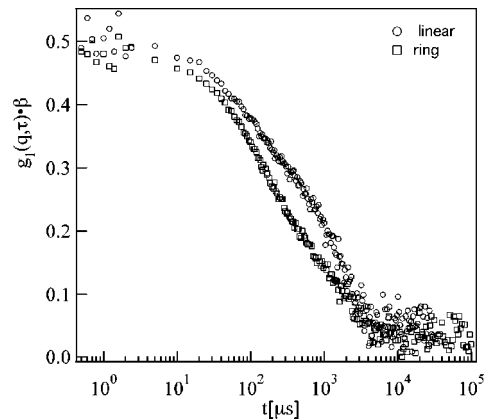


Figure 6. Comparison between the field autocorrelation functions of ring-like and open DNA constructs at $\theta = 70^\circ$. Both relaxation modes are slower for the open nanostructure.

are shown in Table 3 and are in good agreement with those obtained with the double exponential fitting (DEF). Moreover, the average translational diffusion coefficient for the fast population is in excellent agreement with that obtained from Monte Carlo for the ring-like nanoconstructs.

The size distribution extracted from CONTIN analysis of the autocorrelation function for $\theta = 90^\circ$ is reported in Figure 5b as an example. The fast and slow populations seem equivalent, but the weight factor is intensity-weighted, meaning that a small amount of large particles dominates the scattering. As for the amplitude factor P in the double exponential fitting, the relative intensities of the two populations are significantly affected by the angular scale. It is possible to obtain a number-weighted distribution correcting the relative intensities for the form factor and the mass of the particles.^{60,61} A coarse-grained evaluation of the relative abundance can be obtained by modeling both populations as spheres, which yields a qualitative number-

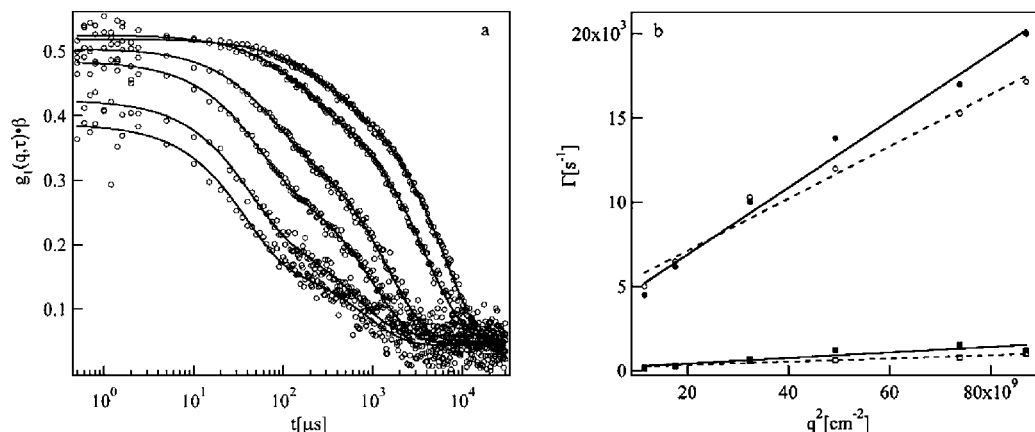


Figure 7. (a) DLS intensity autocorrelation functions of 3 μM DNA open nanostructures at different scattering angles. The double exponential fitting curves are reported as solid lines. (b) Behavior of the relaxation rates from the double exponential fitting and the mean relaxation times from CONTIN as a function of the square scattering vector. The solid curves are the linear fitting to infer the translation diffusion coefficient $D_t = \Gamma/q^2$. (●) Γ_1 (DEF), (■) Γ_2 (DEF), (○) Γ_1 CONTIN, (□) Γ_2 CONTIN.

weighted size distribution⁶² significantly skewed toward the smaller population ($\approx 98\%$) for all scattering angles.

The same DLS investigation has been performed on the linear open analogue. A comparison between the field autocorrelation functions of the ring-like and open nanostructures at $\theta = 70^\circ$ is reported as an example in Figure 6. Both autocorrelation functions are bimodal, but the characteristic relaxation decays are markedly different for the two systems. In particular, both modes for the linear nanostructures are characterized by larger relaxation times than for the ring-like ones. A DLS investigation of 3 μM DNA open objects as a function of the scattering angle (Figure 7a) allows us to determine the translational diffusion coefficients of both populations. The decay rates have been obtained with the aid of a double exponential fitting and the CONTIN inversion method, and their behavior as a function of the square scattering vector is reported in Figure 7b. The diffusion coefficient and the hydrodynamic radii inferred from the two methods are reported in Table 3. The agreement between the two analyses is good, but not so satisfying as for the ring-like structures. This is related to the higher polydispersity (Figure 5b) affecting the size distributions for the linear derivatives, suggesting that the open constructs tend to associate to some extent.

UV Melting. UV melting experiments were performed to highlight differences in the hybridization process of the closed system and the open counterpart. The melting curves and their first derivatives are reported in Figure 8. The temperature behavior of the derivatives almost overlapped for $T > 64^\circ\text{C}$ but significantly differs in the first part of the process. In particular, the ring-like derivative is characterized by a steep first peak at 60°C that is not present in the open counterpart, probably connected to the opening-up of the ring. The same behavior has been previously observed in smaller DNA self-assembled structures, and it has been related to a thermodynamic strain inherent to the closed system due to a significant immobilization entropy.²⁹ Once this strain is released, the melting behavior is identical for the closed and open constructs.

A qualitative calculation of the melting temperatures of the six duplex segments assembled in the closed structures (considered as disjointed duplexes in solution) according to the NNA method has indicated the DD' helix as the weakest side in (Figure 1a) with $T_m = 53^\circ\text{C}$, lower than all the other duplexes. The DD' duplex is also present in the open counterpart, and this strengthens the hypothesis that the observed difference in the first step of the melting process is not due to the lack of

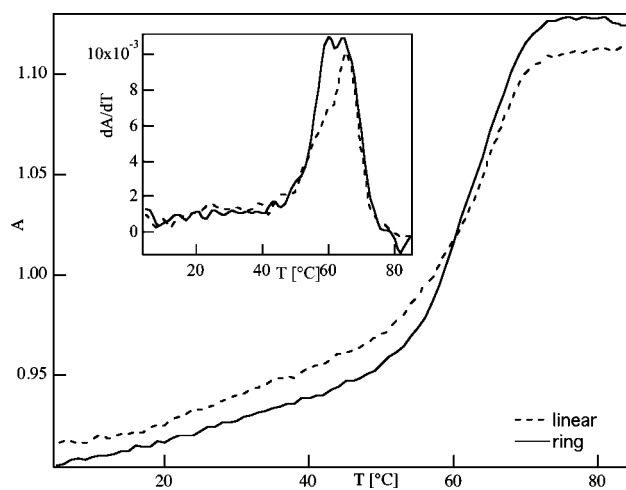


Figure 8. UV melting experiments of 0.3 μM ds-DNA ring-like (solid line) and open (dotted line) constructs. The inset reports the first derivative of the melting curves.

one of the duplexes in the open system (AA'), but rather to different geometric features which are translated in different thermodynamic behavior.

Atomic Force Microscopy. The DNA nanoconstructs were immobilized onto mica for AFM visualization following the procedure reported in the experimental section. AFM measurements in true noncontact mode were performed for thermally annealed solutions of both sequences 1–6A and 1–6B: the results for the two systems are reported separately.

Closed DNA Constructs. Figure 9a shows a typical AFM image of the DNA assemblies deposited from a 1.7 μM solution of sequences 1–6A. The structures appear mainly as isolated disk-shaped domains homogeneously distributed over the surface, with thickness in the range 1.5–6.0 nm. Interestingly, the use of the development procedure⁶³ in ultrapure water allowed us to obtain a homogeneous distribution of isolated oligonucleotide nanodomains over large scan areas, as shown in Figure 9a.

Image analysis was performed on large scan areas in different parts of the mica surface to obtain the distribution fit reported in Figure 9b. We assumed nearly circular shapes for all the observed domains computing the mean geometric radius as $R_m = (2a_{\min} + 2a_{\max})/4$, where a_{\min} and a_{\max} are the minor and major axes, respectively. Typical surface density distribution, Γ_s , of the DNA nanostructures as a function of the average

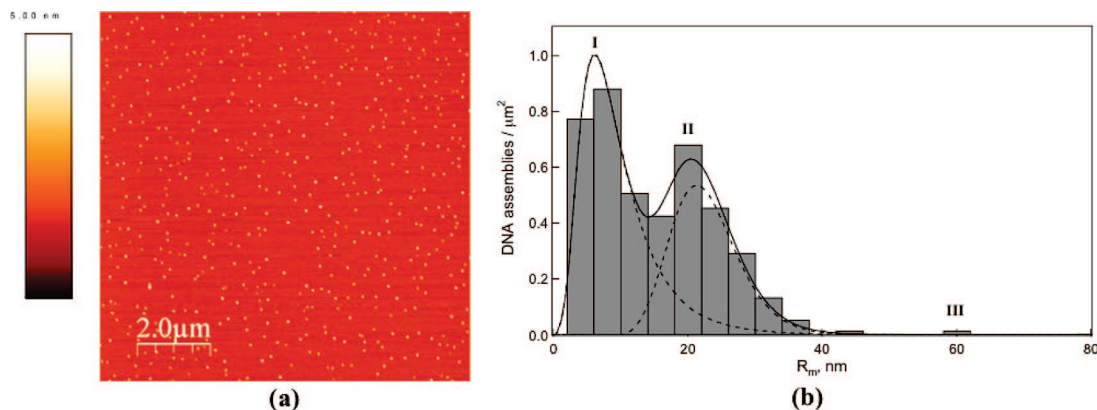


Figure 9. (a) AFM topographic image ($10 \mu\text{m} \times 10 \mu\text{m}$) for closed DNA nanostructures immobilized on mica; (b) density distribution as a function of the average radius, R_m , of the structures. The dashed and solid lines represent the best fit of the data according to eq 6. The surface density of the DNA domains, Γ_s , was estimated as the number of DNA structures divided by the scan area of the sample.

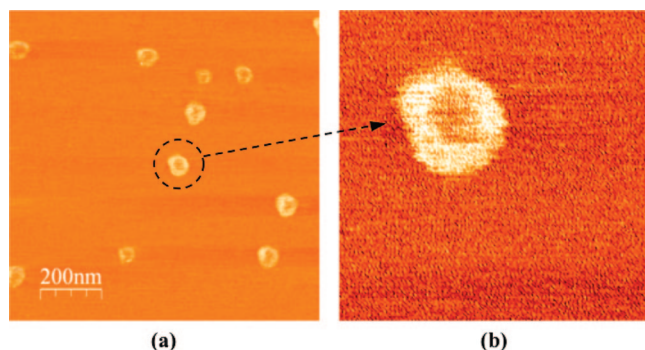


Figure 10. (a) AFM phase image ($1 \mu\text{m} \times 1 \mu\text{m}$) for population I on mica; (b) closeup ($200 \text{ nm} \times 200 \text{ nm}$) of a deformed toroidal single domain.

radius is reported in Figure 9b: the histogram evidenced the presence of two main populations centered at $R_m = 10 \text{ nm}$ (I) and $R_m = 24 \text{ nm}$ (II), respectively. A larger size population (III) with $R_m = 60 \text{ nm}$ is also observed but with a very low surface density representing only 1% of the total immobilized ds-oligonucleotides.

Higher-resolution phase and amplitude AFM images revealed a different behavior for the two populations: a variety of domains with different shape and height are observed for population II, whereas population I consists only of isolated DNA assemblies with a deformed toroidal shape of maximum thickness of 1.7 nm and a central depression of radius of 4–6 nm. Typical results are reported in Figure 10 for the population centered at $R_m = 10 \text{ nm}$ and in Figure 11 for the domains with $R_m = 24 \text{ nm}$. In the latter case, dimers of aligned circular structures (Figure 10a) as well as irregular aggregates (Figure 10b) of ellipsoidal shape were identified. Self-assembly of closed DNA constructs was recently reported also by other authors that observed minicircles of DNA²² and polygonal-shaped structures^{64,65} on mica.

Detailed information on the size and shape of the observed populations was extracted from a nonlinear fitting of the surface density histogram of Figure 11b using eq 6.

The results of the fitting are reported in Table 4 together with the corresponding thickness determined from topographic images; the fraction of the population centered on $R_m = 60 \text{ nm}$ is too small to allow a significant fitting of the experimental data with eq 6. The mean radius for population I is $R_0 = 8.3 \text{ nm}$ and the width of the size distribution spans from $R_l = 4.8 \text{ nm}$ to $R_r = 14.4 \text{ nm}$. The measured thickness of 1.7 nm is in good agreement with the literature values of 1.4–1.8 found for

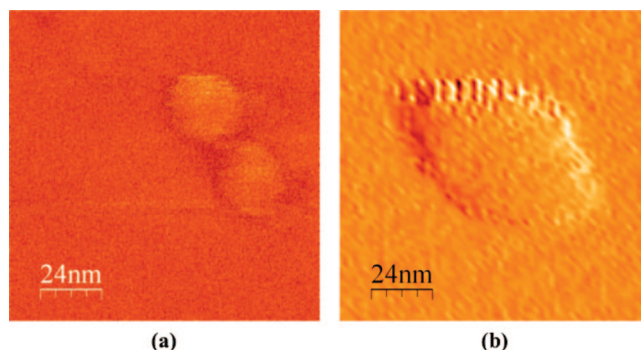


Figure 11. AFM phase image ($120 \text{ nm} \times 120 \text{ nm}$) for two typical examples of DNA domains with $R_m = 24 \text{ nm}$ on mica: (a) dimers of circular structures, (b) higher aggregates.

TABLE 4: Lateral Size and Height Parameters of Closed Constructs

	R_0, nm^a	f	Γ_s , DNA assemblies μm^{-2}	average thickness, nm
population I	8.3 ± 0.3	1.74	2.59 ± 0.06	1.7 ± 0.3
population II	22.3 ± 0.2	1.26	1.68 ± 0.08	3.5 ± 1.5
population III	50–60		0.03	6–8

^a R_0 = mean radius calculated from eq 6. The indicated errors correspond to the standard deviation of the mean value and were obtained from eq 6. For population III, R_m was estimated from the histogram representation of Figure 11b.

isolated DNA double strands measured by AFM in noncontact or soft contact mode.^{48,49,66–68}

The larger nanoconstructs of population II have a mean radius of 22.3 nm and the distribution is only slightly asymmetric. The thickness of these structure spans from 2 to 4.5 nm suggesting the presence of a variety of DNA assemblies organization: pairs of closed structures (Figure 11a), partially superimposed circular structures each with the thickness of a double strand (Figure 11b), and intermediate situations. The comparison between the surface density for populations I and II reveals that there is a higher tendency to form isolated DNA nanoconstructs rather than dimers or higher composed structures. The small population III is constituted by irregularly shaped aggregates with a lateral dimension of 100–120 nm and with a maximum thickness that ranges from 6 to 8 nm. Such structures may arise from DNA aggregates already present in solution and partly from surface-induced aggregation favored by the presence of the divalent cations.

TABLE 5: Circularity of the DNA Assemblies Observed for the Closed Constructs

	DNA nanostructure shape	theoretical circularity ^a	circularity, <i>c</i>
population I	pseudo-hexagonal DNA constructs	0.91	0.90 ± 0.01
population II	aligned dimers	0.60	0.66 ± 0.03
	ellipsoidal domains	0.85	
population III	irregular domains		0.60 ± 0.10

^a The theoretical circularity was computed assuming a perfect hexagon for population I and ellipsoidal structures for populations II and III. In the case of population II, theoretical circularity was computed using the experimental dimensions for the minor and major axes of the ellipse (see Supporting Information) in Figures 10 and 11.

TABLE 6: Lateral Size and Height Parameters of Open DNA Structures Observed on Mica

	height analysis		size analysis	
	Γ _s , DNA assemblies μm ⁻²	average thickness, nm	W _{max,nm} (w ^a)	W _{min,nm} (w ^a)
population I	4 ± 1	1.4 ± 0.1	38 ± 1 (54)	20 ± 1 (38)
population II	2 ± 1	2.9 ± 0.3		
population III	0.8 ± 0.4	4.5 ± 1.8	100 ^b	60 ^b

^a *w* is the width at half-maximum of the distribution fit by using eq 6. ^b The long axis fit is not satisfactory above 80 nm inducing an underestimate of the long axis for population III, the dimensions in parenthesis are taken from visual inspection of AFM images.

Further analysis of the AFM images provided the circularity parameter reported in Table 5 for each of the observed DNA nanoconstructs. Circularity *c* is defined as

$$c = \frac{4\pi A}{p^2} \quad (10)$$

where *A* and *p* are the area and the perimeter of each domain.

The experimentally determined values of *c* are reported in Table 5 together with the expected theoretical predictions for the various DNA structures (see Supporting Information). In the case of population I, we computed the expected circularity value assuming both a circular and hexagonal geometry obtaining *c* = 1 and *c* = 0.91, respectively. The experimental *c* value is much closer to a hexagonal shape than a perfect circle evidencing the presence of slightly deformed circles or more probably “quasi” polygonal constructs. For the ellipsoidal domains of population II, we used the dimensions evaluated for the two extreme cases reported in Figures 10 and 11: isolated pairs of DNA structures and aggregated domains. The experimental *c* value falls in the range between the two examples, although it indicates the presence of a majority of elongated structures. For population III, the experimental circularity corresponds to even more elongated domains.

Open DNA Constructs. Figure 12a shows a representative height image of DNA constructs deposited from a 1.7 μM solution of 1–6B sequences; we always observed irregularly shaped particles covering the surface, although AFM experiments were less reproducible than in the case of the closed DNA system.

The DNA domains differ in shape and height, as can be seen by the maximum thickness distribution in Figure 12b. The distribution peak corresponds to 2-nm-thick domains, but a large fraction of DNA constructs with maximum thickness close to 3 nm is also observed. Moreover, a small but significant

population constituted of 3D aggregated materials 4 to 6 nm high (see Figure 12b) is also present.

High-resolution AFM images evidenced DNA elongated structures with dimensions of 50–80 nm and 20–30 nm for the major and the minor axes, respectively. AFM images for two representative elongated structures are reported in Figure 13 together with an example of a larger aggregate with higher thickness.

The height profile along the major and minor axes is also described in Figure 13: whereas for the large aggregates (Figure 13c), we always observe a homogeneous thickness of 4 nm for both axis, in the case of the elongated structures (Figure 13a,b), the height along the major axis shows a two-step profile. The thickness of each step is 1.3–1.5 nm, a value close to the AFM thickness of a single DNA double strand.^{49,66,69} Such behavior may be explained by considering the elongated structures as formed by two discrete DNA tiles that overlap, to different extents, one on top of the other, reaching a maximum thickness of 2.0–3.0 nm. Each DNA tile has the short axis in the range 20–25 nm and the long axis close to 50 nm, the tile is probably formed by several aligned DNA double strands (8–10) interacting with each other to form partially superimposed dimers along the *z* direction.

We analyzed the size distribution obtained from AFM measurements assuming that all populations described in Figure 12 are ellipsoidal in shape using eq 6. The results of the distribution fit are summarized in Table 6 both for the height and the lateral size distribution. The data show that the highest fraction of DNA constructs is present as single tiles or pairs of DNA tiles with little overlap; totally superimposed structures (see Figure 13) are less frequent.

Similarly to DLS experiments, AFM results showed the presence of a small fraction of larger aggregates (population III) consisting of several layers of DNA double strands with average length of 100 nm (see Figure 13c) although the presence of the Mg²⁺ ions may further enhance the aggregation process compared to solution behavior.

Discussion

The major features (shape and conformation) of closed and open DNA nanostructures formed in solution from two 20-mer strands joined by a double thymine junction have been obtained from Monte Carlo simulations. Closed objects deviate from a circular shape and are characterized by a relatively high flexibility, provided by the nonpairing TT sequences that, according to the molecular design, act as hinges between rigid ds sides. It is instructive to compare the calculated diffusion coefficients of both nanostructures obtained from Monte Carlo to those obtained experimentally by DLS.

DLS autocorrelation functions of ring-like and linear systems show two well-separated relaxation rates. In particular, ring-like constructs (resembling to deformed hexagonal structures) are characterized by faster relaxation times than the linear ones for both populations as clearly shown in Figure 7. The hydrodynamic size of the ring-like nanostructures related to the fast mode is in agreement with the expected dimension for the desired DNA nanostructures, while the slow decays are consistent with the presence of aggregation products. A qualitative estimation of the number-weighted distribution of the two populations shows that the faster one represents about the 98% of the self-assembled objects. The average experimental diffusion coefficient of the ring-like nanostructure is 2.8 × 10⁻⁷ cm²/s at 20 °C: this value is in excellent agreement with the diffusion coefficient calculated for the equilibrium structure obtained at

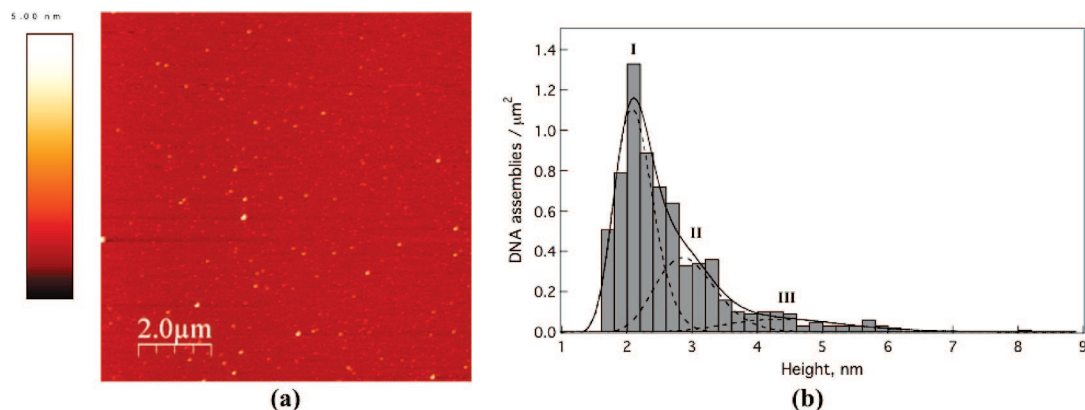


Figure 12. (a) Topographic image of a $10\ \mu\text{m} \times 10\ \mu\text{m}$ scan range for open nanostructures on mica; (b) density distribution as a function of the maximum thickness of the structures. The solid and dashed lines represent the best fit of the data according to eq 6.

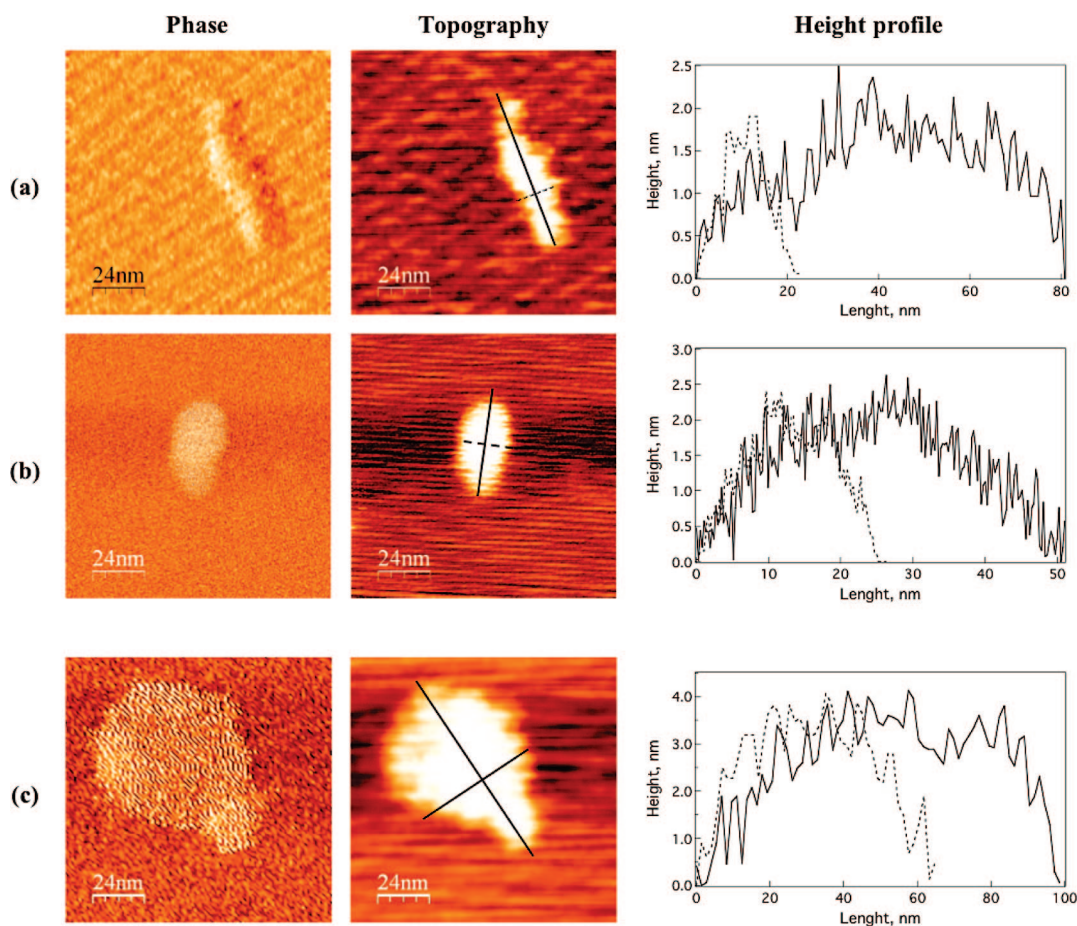


Figure 13. Phase and topographic AFM images ($120\ \text{nm} \times 120\ \text{nm}$) together with the height profile along the major and minor axes of different structures anchored on mica: (a) partially superimposed elongated structure, (b) totally superimposed elongated structure, (c) larger aggregate.

the same temperature from Monte Carlo simulations (Table 2). AFM investigation shows that on the surface 60% of the particles look like isolated ring objects (Figure 10a) with a radius $R_0 = 8.3\ \text{nm}$ whose circularity is very close to that of an hexagonal object. This indicates that, although characterized by high flexibility in solution, due to the TT junctions as shown by the simulations, they are not deformed as prolate or oblate objects (whose circularity would be much lower), but exhibit the expected hexagonally shaped structure. For these pseudohexagonal constructs, the resulting radius is slightly larger than the one from MC results; this is probably due to the squeezing effect from the tip interaction.^{43,44,70} An overlap of a representative AFM image, obtained for the isolated structures, with the

simulated one (Figure 14), highlights a very good agreement, showing that the programmed sequences, 1–6A, efficiently self-assemble in pseudohexagonal constructs, whose shape and size can be predicted well by Monte Carlo simulations. AFM analysis has also shown that the 39% of the pseudohexagonal particles associate to form dimers or elliptic aggregates whose dimensions are about 40 nm (Figure 11a,b). Such structures can be observed as larger objects as accounted by the first population of particles in DLS (Figure 5b), even if in this case their percentage is lower. It is reasonable to speculate that, once deposited on mica, the hexagon association to form larger aggregates is enhanced by the presence of Mg^{2+} . Larger aggregates of irregular shape, about 1% of the total immobilized ds-oligonucleotides, have

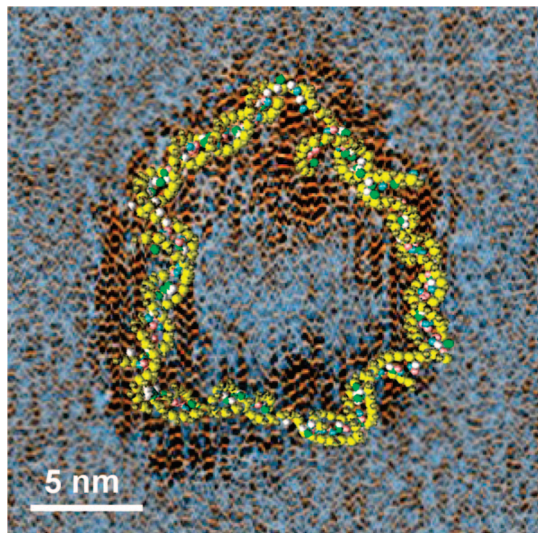


Figure 14. Representation of the experimental AFM image of an isolated DNA pseudo-hexagonal nanostructure overlapped with the equilibrium conformation at 20 °C obtained for the same DNA sequence from Monte Carlo simulation.

been also detected, and they can be related to the slowest population observed in DLS and probably represent some undesired polymerization products from the annealing procedure.

The experimental diffusion coefficients of linear nanostructures, extracted with the two different analysis methods, differ by 20% indicating a higher polydispersity for this system (Figure 5b). Moreover, the average diffusion coefficient (Table 3), $\langle D_t \rangle$, is slightly underestimated with respect to the calculated one for an isolate chain (Table 2). These results suggest that, for the linear nanoconstructs, the isolated structures, which are responsible for the fast relaxation, prevail, but they tend to associate (lowering the average diffusion coefficient) leading to this underestimation. All these findings support that open DNA assemblies tend to associate to a larger extent in solution than the closed counterpart that can therefore be considered a more stable structure. Moreover, aggregation seems to be strongly enhanced by deposition on a surface, as shown by AFM images, where the most representative structures are elongated tiles, probably composed of several open nanoconstructs aligned together. Pairs of such DNA tiles tend to superimpose to different extent as shown in two representative cases of Figure 13. Although open nanostructures are prone to associate in solution as well, we believe that this process is significantly promoted by the presence of Mg^{2+} cations^{71,72} used for surface immobilization. However, aggregation of DNA assemblies induced by divalent cations is found to be more effective for the open structures than for pseudo-hexagonal objects. This can be due to geometrical constraints, but also to the fact that cations generally show a higher condensation efficiency on single-stranded DNA,⁷³ and open nanostructures are composed of single-stranded DNA (62 bp) to larger extent than the closed objects (18 bp).

Finally, as already shown for similar smaller DNA assemblies,²⁹ UV melting behavior seems to be significantly affected by geometrical constraints. Monte Carlo simulations of both nanostructures abruptly brought at 70 °C allows us to follow the ring rupture process and compare it to the melting behavior of the open architecture. Both nanostructures start breaking along the DD' double helix side (see Figure 1), but this first opening process occurs more quickly and at lower temperature for the pseudo-hexagonal structure that, once broken,

assumes a conformation similar to the open analogue. These findings are in good agreement with the experimental melting behavior and strengthen the hypothesis that the first sharp peak in the melting curve of the cyclic structure is related to the closed conformation, where an initial unbinding between base pairs is decisive for the complete opening of the structure.

Conclusions

A combined DLS and AFM analysis, supported by Monte Carlo simulations, has shown that the designed linear oligonucleotides 1–6A (see Table 1) successfully self-assemble to form the desired 7 nm pseudo-hexagonal nano-objects in a pretty high yield. Monte Carlo simulations and experimental findings have shown that the insertion of double thymine hinges imparts to the system the required flexibility. Analogue DNA open nanostructures have also been characterized as a control, and they were found to form aggregates of the primary nanoconstructs at a larger extent than pseudo-hexagons, both in solution and once immobilized on the surface. Hence, stable hexagonally shaped nanoconstructs can be exploited to perform a programmable surface coverage to build up more complex self-assembling systems. In this study, we have also demonstrated that DLS, providing a dynamic and structural analysis of such self-assemblies, represents a very efficient screening technique to discriminate DNA nanostructures of different shape and/or size in situ without modifying or transferring the sample to another medium, namely, a gel.

Acknowledgment. The authors would like to acknowledge John Tumpane for the experimental UV-melting curves on the 22-mer nanostructures. The authors acknowledge EU-STREP program (project reference AMNA, Contract No. 013575), MiUR (Prin 2006), and CSGI/CNR - Fusint project for financial support.

Supporting Information Available: Additional experimental information as described in the text. This material is available free of charge via the Internet at <http://pubs.acs.org>.

References and Notes

- (1) Berti, D.; Barbaro, P. L.; Buccini, I.; Baglioni, P. *J. Phys. Chem. B* **1999**, *103*, 4916.
- (2) Baglioni, P.; Berti, D. *Curr. Opin. Colloid Interface Sci.* **2003**, *8*, 55.
- (3) Baldelli Bombelli, F.; Berti, D.; Almgren, M.; Karlsson, G.; Baglioni, P. *J. Phys. Chem. B* **2006**, *110*, 17627.
- (4) Banchelli, M.; Berti, D.; Baglioni, P. *Angew. Chem.* **2007**, *46*, 3070.
- (5) Milani, S.; Baldelli Bombelli, F.; Berti, D.; Dante, S.; Hauss, T.; Baglioni, P. *Biophys. J.* **2006**, *90*, 1260.
- (6) Milani, S.; Baldelli Bombelli, F.; Berti, D.; Baglioni, P. *J. Am. Chem. Soc.* **2007**, *129*, 11664.
- (7) Seeman, N. C. *J. Theor. Biol.* **1982**, *99*, 237.
- (8) Chen, J.; Seeman, N. C. *Nature* **1991**, *350*, 631.
- (9) Zhang, Y.; Seeman, N. C. *J. Am. Chem. Soc.* **1994**, *116*, 1661.
- (10) Shih, W. M.; Quispe, J. D.; Joyce, G. F. *Nature* **2004**, *427*, 618.
- (11) Erben, C. M.; Goodman, R. P.; Turberfield, A. J. *J. Am. Chem. Soc.* **2007**, *129*, 6992.
- (12) Winfree, E.; Liu, F.; Wenzler, L.; Seeman, N. C. *Nature* **1998**, *394*, 539.
- (13) LaBean, T. H.; Yan, H.; Kopatsch, J.; Liu, F.; Winfree, E.; Reif, J. H.; Seeman, N. C. *J. Am. Chem. Soc.* **2000**, *122*, 1848.
- (14) Yan, H.; Park, S. H.; Finkelstein, G.; Reif, J. H.; LaBean, T. H. *Science* **2003**, *301*, 1882.
- (15) He, Y.; Tian, Y.; Chen, Y.; Deng, Z.; Ribbe, A. E.; Mao, C. *Angew. Chem. Int. Ed.* **2005**, *44*, 6694.
- (16) Chelyapov, N.; Brun, Y.; Gopalkrishnan, M.; Reishus, D.; Shaw, B.; Adleman, L. *J. Am. Chem. Soc.* **2004**, *126*, 13924.
- (17) Reishus, D.; Shaw, B.; Brun, Y.; Chelyapov, N.; Adleman, L. *J. Am. Chem. Soc.* **2005**, *127*, 17590.
- (18) Park, S. H.; Finkelstein, G.; LaBean, T. H. *J. Am. Chem. Soc.* **2007**, *130*, 40.

- (19) Park, S. H.; Pistol, C.; Ahn, S. J.; Reif, J. H.; Lebeck, A. R.; Dwyer, C.; LaBean, T. H. *Angew. Chem. Int. Ed.* **2006**, *45*, 735.
- (20) Park, S. H.; Yin, P.; Liu, Y.; Reif, J. H.; LaBean, T. H.; Yan, H. *Nano Lett.* **2005**, *5*, 729.
- (21) Aldaye, F. A.; Sleiman, H. F. *Angew. Chem. Int. Ed.* **2006**, *45*, 2204.
- (22) Rasched, G.; Ackermann, D.; Schmidt, T. L.; Broekmann, P.; Heckel, A.; Famulok, M. *Angew. Chem. Int. Ed.* **2008**, *47*, 967.
- (23) Tumpene, J.; Kumar, R.; Lundberg, E. P.; Sandin, P.; Gale, N.; Nandhakumar, I. S.; Albinsson, B.; Lincoln, P.; Wilhelmsson, L. M.; Brown, T.; Norden, B. *Nano Lett.* **2007**, *129*, 6859.
- (24) Betti, F.; Baldelli Bombelli, F.; Gambinossi, F.; Caminati, G.; Brown, T.; Baglioni, P.; Berti, D. submitted for publication, 2008.
- (25) Mirkin, C. A.; Letsinger, R. L.; Mucic, R. C.; Storhoff, J. J. *Nature* **1996**, *382*, 607.
- (26) Alivisatos, A. P.; Johnsson, K. P.; Peng, X. G.; Wilson, T. E.; Loweth, C. J.; Bruchez, M. P.; Schultz, P. G. *Nature* **1996**, *382*, 609.
- (27) Nykypanchuk, D.; Maye, M. M.; van der Lelie, D.; Gang, O. *Nature* **2008**, *451*, 549.
- (28) Park, S. Y.; Lytton-Jean, A. I. K.; Lee, B.; Weigand, S.; Schatz, G.; Mirkin, C. A. *Nature* **2008**, *451*, 553.
- (29) Tumpene, J.; Sandin, P.; Kumar, R.; Powers, V. E. C.; Lundberg, E. P.; Gale, N.; Baglioni, P.; Lehn, J.-M.; Albinsson, B.; Lincoln, P.; Wilhelmsson, L. M.; Brown, T.; Norden, B. *Chem. Phys. Lett.* **2007**, *440*, 125.
- (30) Tsai, C. J.; Zheng, J.; Aleman, C.; Nussinov, R. *Trends Biotechnol.* **2006**, *24*, 449.
- (31) Yingling, Y. G.; Shapiro, B. A. *Nano Lett.* **2007**, *7*, 2328.
- (32) Knotts, T. A.; Rathore, N.; Schwartz, D. C.; de Pablo, J. J. *J. Chem. Phys.* **2007**, *126*, 084901.
- (33) Drukker, K.; Schatz, G. C. *J. Phys. Chem. B* **2000**, *104*, 6108.
- (34) Sales-Pardo, M.; Guimera, R.; Moreira, A. A.; Widom, J.; Amaral, L. A. N. *Phys. Rev. E* **2005**, *71*, 051902.
- (35) Arnott, P. J. S.; Smith, C.; Chandrasekaran, R. Atomic Coordinates and Molecular Conformations for DNA-DNA, RNA-RNA, and DNA-RNA Helices. In *CRC Handbook of Biochemistry and Molecular Biology*; 3rd ed.; CRC Press: Cleveland, 1976; Vol. 2; pp 411.
- (36) Hoang, T. X.; Cieplak, M. *J. Chem. Phys.* **2000**, *112*, 6851.
- (37) Pastre, D.; Pietrement, O.; Fusil, S.; Landousy, F.; Jeusset, J.; David, M.-O.; Hamon, L.; Le Cam, E.; Zozime, A. *Biophys. J.* **2003**, *85*, 2507.
- (38) Pietrement, O.; Fusil, S.; Jeusset, J.; David, M. O.; Landousy, F.; Hamon, L.; Zozime, A.; Le Cam, E. *Langmuir* **2003**, *19*, 2536.
- (39) Hansma, H. G.; Laney, D. E. *Biophys. J.* **1996**, *70*, 1933.
- (40) Fang, Y.; Hoh, J. H. *FEBS Lett.* **1999**, *459*, 173.
- (41) Lio, A.; Charych, D. H.; Salmeron, M. *J. Phys. Chem. B* **1997**, *101*, 3800.
- (42) Abdelhady, H. G.; Allen, S.; Davies, M. C.; Roberts, C. J.; Tendler, S. J. B.; Williams, P. M. *Nucleic Acids Res.* **2003**, *31*, 4001.
- (43) Bustamante, C.; Vesenska, J.; Tang, C. L.; Rees, W.; Guthold, M.; Keller, R. *Biochemistry* **1992**, *31*, 22.
- (44) Vesenska, J.; Guthold, M.; Tang, C. L.; Keller, D.; Delaine, E.; Bustamante, C. *Ultramicroscopy* **1992**, *42–44*, 1243.
- (45) Hansma, H. G. *Annu. Rev. Phys. Chem.* **2001**, *52*, 71.
- (46) Song, Y.; Li, Z.; Liu, Z.; Wei, G.; Wang, L.; Sun, L.; Guo, C.; Sun, Y.; Yang, T. *J. Phys. Chem. B* **2006**, *110*, 10792.
- (47) Nakayama, Y.; Tanaka, H.; Kawai, T. *Jpn. J. Appl. Phys.* **2001**, *40*, L824.
- (48) Davies, E.; Teng, K. S.; Conlan, R. S.; Wilks, S. P. *FEBS Lett.* **2005**, *579*, 1702.
- (49) Maeda, Y.; Matsumoto, T.; Kawai, T. *Appl. Surf. Sci.* **1999**, *140*, 400.
- (50) Horcas, I.; Fernandez, R.; Gomez-Rodriguez, J. M.; Colchero, J.; Gomez-Herrero, J.; Baro, A. M. *Rev. Sci. Instrum.* **2007**, *78*, 013705.
- (51) Villarrubia, J. S. *J. Res. Natl. Inst. Stand. Technol.* **1997**, *102*, 425.
- (52) Abramoff, M. D.; Magalhaes, P. J.; Ram, S. J. *Biophotonics International* **2004**, *11*, 36.
- (53) Grosberg, A. Y.; Khokhlov, A. R. *Statistical Physics of Macromolecules*; Springer: Berlin, 1997.
- (54) Jang, S. S.; Çagin, T.; Goddard, W. A., III. *J. Chem. Phys.* **2003**, *119*, 1843.
- (55) Lankas, F.; Lavery, R.; Maddocks, J. H. *Structure* **2006**, *14*, 1527.
- (56) Kawaguchi, T. *J. Appl. Crystallogr.* **2001**, *34*, 580.
- (57) Thaokar, R. M. *Colloids Surf.* **2008**, *317*, 650.
- (58) Muthukumar, M. J. *Chem. Phys.* **1997**, *107*, 2619.
- (59) Berne, B. J.; Pecora, R. *Dynamic Light Scattering*; John Wiley & Sons: New York, 1976.
- (60) Hallett, F. R.; Craig, T.; Marsh, J.; Nickel, B. *Can. J. Spectrosc.* **1989**, *34*, 63.
- (61) Pencer, J.; White, G. F.; Hallett, F. R. *Biophys. J.* **2001**, *81*, 2716.
- (62) Bohren, C. F.; Huffman, D. R. In *Absorption and Scattering of Light by Small Particles*; John Wiley & Sons: New York, 1983.
- (63) Song, Y.; Guo, C.; Sun, L.; Wei, G.; Peng, C.; Wang, L.; Sun, Y.; Li, Z. *J. Phys. Chem. B* **2007**, *111*, 461.
- (64) Asakawa, T.; Nishi, K.; Mizuno, R.; Yoneda, K.; Okada, T.; Hayashi, K. *Thin Solid Films* **2006**, *509*, 85.
- (65) Mizuno, R.; Haruta, H.; Morii, T.; Okada, T.; Asakawa, T.; Hayashi, K. *Thin Solid Films* **2004**, *464–465*, 459.
- (66) Moreno-Herrero, F.; Colchero, J.; Baro, A. M. *Ultramicroscopy* **2003**, *96*, 167.
- (67) Rouillat, M. H.; Dugas, V.; Martin, J. R.; Phaner-Goutorbe, M. *Appl. Surf. Sci.* **2005**, *252*, 1765.
- (68) Yang, C.-W.; Hwang, I.-S.; Chen, Y. F.; Chang, C. S.; Tsai, D. P. *Nanotechnology* **2007**, 084009.
- (69) Winfree, E.; Liu, F.; Wenzler, L. A.; Seeman, N. C. *Nature* **1998**, *394*, 539.
- (70) Fung, S. Y.; Keyes, C.; Duhamel, J.; Chen, P. *Biophys. J.* **2003**, *85*, 537.
- (71) Sha, F.; Mu, R.; Henderson, D.; Chen, F.-M. *Biophys. J.* **1999**, *77*, 410.
- (72) Costa, L. T.; Kerkmann, M.; Hartmann, G.; Endres, S.; Bisch, P. M.; Heckl, W. M.; Thalhammer, S. *Biochem. Biophys. Res. Commun.* **2004**, *313*, 1065.
- (73) Costa, D.; Miguel, M. G.; Lindman, B. *J. Phys. Chem. B* **2007**, *111*, 10886.

JP804544U